Analysis of bistability conditions between lasing and nonlasing states for a vertical-cavity surface-emitting laser with frequency-selective optical feedback using an envelope approximation

A. V. Naumenko and N. A. Loiko
Institute of Physics, Academy of Sciences of Belarus, 68 Nezalezhnasti ave., 220072 Minsk, Belarus

T. Ackemann*
SUPA and Department of Physics, University of Strathclyde, 107 Rottenrow, Glasgow G4 ONG, Scotland, United Kingdom
(Received 21 November 2006; published 2 August 2007)

The emission characteristics of a vertical-cavity surface-emitting laser (VCSEL) coupled to an external cavity with a diffraction grating as a frequency-selective element are theoretically analyzed. We introduce envelope functions for the set of external-cavity modes based on the loci of modes with extremal gain or frequency in the proper parameter space. Replacing the set of discrete stationary solutions by these envelope functions, simple analytical expressions are derived for the existence of bistability between a lasing state strongly affected by the feedback and a state close to the solitary laser emission (in particular the nonlasing state) and for the frequency of the VCSEL in the grating-controlled regime. It is shown how the initial jump of the laser intensity during abrupt turn-on can be maximized. By a control of the feedback change, the width of the hysteresis loop can be increased significantly. The scheme under consideration can be useful in all-optical photonic switching applications.

DOI: 10.1103/PhysRevA.76.023802 PACS number(s): 42.65.Pc, 42.55.Px, 42.60.Mi, 42.65.Sf

I. INTRODUCTION

This paper is devoted to theoretical investigations of the influence of delayed spectrally filtered optical feedback on the operation characteristics of a vertical-cavity surface-emitting laser (VCSEL). In edge-emitting semiconductor lasers, external frequency-selective optical feedback along is known to provide stabilization of single-longitudinal mode operation [1–4] but also to induce bi- or multistability between different emission states of the laser [5–9]. In particular, in Ref. [7] a filter-induced bistability between solitary laser and external cavity states was observed.

Bistability between lasing and nonlasing states and as a result an abrupt turn-on at threshold was studied experimentally and theoretically in a recent paper for a VCSEL with optical feedback from a diffraction grating [10]. The bistability arises due to the interplay of the frequency selectivity of the grating, phase-amplitude coupling and thermal shifts of the emission frequency. In this paper, we are going to provide an analytical treatment of these phenomena. In particular, we will consider the conditions for the existence of on-off bistability and abrupt turn-on, estimate the rate of frequency shift in the grating-controlled regime, and readdress the stability analysis of the system and how stability properties can be tailored by a suitable control of the feedback phase. The results could serve as guidelines for new experiments and for the design of optimized devices.

This type of bistability could be useful for all-optical switching in photonic applications. In broad-area devices, the bistable characteristic might give rise spatial self-localized emission states (cavity solitons) [11], which are considered as "bits" in future all-optical information processing schemes [12]. Also, frequency-selective feedback provides additional possibilities for the design of laser schemes with higher controllability in comparison to conventional external optical feedback (e.g., for chaotic encryption applications), especially in conjunction with polarization degrees of freedom.

II. MODEL

Polarization and spin dynamics of a VCSEL based on a quantum-well active medium can be described in framework of the so-called spin-flip-model (SFM) [13]. The modified rate equations describing the polarization dynamics in a VCSEL with frequency selective optical feedback from a distant diffraction grating have the following form [10]:

$$\frac{d}{dt}\bar{E} = \hat{G}\cdot\bar{E} + \bar{F} + \bar{W}_E,$$

$$\frac{d}{dt}\bar{N} = \bar{\mu} + \hat{S}\cdot\bar{I} - \bar{W}_N. \tag{1}$$

Here, the components of the column vector $\bar{E}\equiv(E_+,E_-)$ denote the slowly varying amplitudes of the left and right circularly polarized components of the optical field; $\bar{E}_{opt}(t) = \mathrm{Re}(\bar{E}(t)\exp(i\omega_0 t))$, where ω_0 is an arbitrary reference frequency. They are connected to the $\hat{x}$- and $\hat{y}$-linearly polarized components of the field E_x and E_y by $E_\pm = (1/\sqrt{2})(E_x \pm iE_y)$. We introduce also formal vectorial notations $\bar{I}$, $\bar{N}$ and $\bar{\mu}$ in order to write the material equations in a compact form. Thus, $\bar{I}\equiv(|E_+|^2,|E_-|^2)$ represents the intensity. The vector $\bar{N}\equiv(N,D)$ represents the carrier populations, where N is the total population difference between the conduction and va-

*Formerly at Institute for Applied Physics, University of Münster, Germany.

lence bands, D is the difference of the population differences for the two allowed transitions between the magnetic sublevels associated with right and left circularly polarized light. The vector $\bar{\mu} \equiv [\Gamma(\mu - N), -\gamma_s D]$ represents pumping and relaxation processes, where μ is the normalized injection current, which takes the value 1 at the solitary laser threshold. γ_s is the decay rate for the difference D which is reduced by both spontaneous emission and spin-flip relaxation processes, Γ is the decay rate of the total carrier population N (we use a typical value of $1/\Gamma \equiv \tau_e = 1$ ns). The matrices

$$\hat{G} = \begin{pmatrix} \kappa(1+i\alpha)(N_+ - 1) + i\Delta\omega_0 & -\gamma \\ -\gamma & \kappa(1+i\alpha)(N_- - 1) + i\Delta\omega_0 \end{pmatrix}, \tag{2}$$

$$\hat{S} = -\Gamma \begin{pmatrix} N_+ & N_- \\ N_+ & -N_- \end{pmatrix}, \tag{3}$$

describe gain, nonlinear refractive index and relaxation processes. Here, $N_\pm = N \pm D$ are the population differences for the two allowed transitions. $\gamma = \gamma_a + i\gamma_p$ denotes the anisotropies. γ_a is the anisotropy of the field loss rate (positive γ_a gives the $\hat{y}$-polarized component a lower threshold). γ_p represents the linear birefringence of the cavity (which gives opposite frequency shifts for the different linearly polarized fields of the solitary laser). κ is the mean of the decay rates of the two linearly polarized components of the field; α is the linewidth enhancement factor. $\Delta\omega_0$ is the solitary laser frequency, which is measured—as all optical frequencies—with respect to the reference frequency ω_0. Due to the shift of the cavity resonance because of joule heating, the solitary laser frequency has the following phenomenological dependence on the injection current (see, e.g., [8,9]):

$$\Delta\omega_0 = \Delta\omega_0^{\text{th}} - k_\mu(\mu - 1), \tag{4}$$

where $\Delta\omega_0^{\text{th}}$ is the value of the frequency at the onset of lasing and the coefficient k_μ can be obtained from experiments [corresponding experimentally observed value $k_J = (k_\mu/2\pi)/J_{\text{th}}$ and J_{th} is the solitary laser threshold current]. The effect of filtered feedback from a diffraction grating is calculated as

$$\bar{F}(t) = \frac{1}{2\pi}\int_{-\infty}^{+\infty} d\omega\, \hat{K}(\omega) \int_{-\infty}^{+\infty} dt' \bar{E}(t') \exp[i\omega(t - t')], \tag{5}$$

where $\hat{K}(\omega)$ is the full matrix transfer function of the external cavity. Only one field round-trip in the external cavity is considered here. The polarization principal axes of the grating are aligned with the ones of the VCSEL, but the diffraction efficiency is anisotropic. The operation frequency of the laser with feedback will be denoted by Ω. Hence, the transfer function can be represented as

$$\hat{K}(\Omega) = \hat{\sigma} h(\Omega) \exp[-i\tau(\Omega + \omega_0)], \tag{6}$$

where τ is the external cavity round-trip time, and

$$\hat{\sigma} = \frac{1}{2}\begin{pmatrix} \sigma_x + \sigma_y & \sigma_x - \sigma_y \\ \sigma_x - \sigma_y & \sigma_x + \sigma_y \end{pmatrix}. \tag{7}$$

Here, $\sigma_{x,y}$ represent the feedback strength for the x- and y-polarized components, where $\sigma_{x,y} = (1 - r_2^2) r_{x,y}/(r_2 \tau_{in})$. r_2 is the amplitude reflectivity of the outcoupling mirror of the VCSEL and $r_{x,y}$ are the corresponding values for the grating (on peak) for the two orthogonal polarization components, τ_{in} is the VCSEL cavity round-trip time. $h(\Omega)$ is a normalized frequency dependent part of the transfer function. For the Littman configuration considered in the experiment described in [10] the light emitted by the VCSEL undergoes a double reflection from the diffraction grating before returning into the laser. Hence, the transfer function $h(\Omega)$ is given as square of a normalized reflection coefficient of the grating:

$$h(\Omega) = \left(\exp[-iT(\Omega - \omega_m)] \frac{\sin T(\Omega - \omega_m)}{T(\Omega - \omega_m)} \right)^2. \tag{8}$$

Here, ω_m is the frequency of the main grating maximum. $1/T$ is the grating bandwidth. It is related to the half width at half maximum (HWHM) of the double-reflection transfer function $h(\Omega)$, Eq. (8), by $T = x_0/\text{HWHM}$, where x_0 is the root of the equation $(\sin x_0/x_0)^4 = 1/2$ and $x_0 \simeq 1.0019$. For an arbitrary filter with a profile described by the normalized function $\Pi(w)$ (see the Appendix for details), the corresponding value of x_0 for the determination of the HWHM can be obtained from the equation: $\Pi^2(x_0) = 1/2$.

For the use in simulations, the above integral equation for the feedback term $\bar{F}(t)$ is reformulated as a system of differential equations with delay terms. Making use of the fact that the Green function describing the effects of a single reflection from the grating is $G(t) = \exp(i\omega_m t)[\text{sgn}(t) - \text{sgn}(t - 2T)]/(4T)$ (see, e.g., [9]), the double reflection from the grating can be described by two coupled differential equations [10]:

$$\frac{d}{dt}\bar{F}_1(t) = \frac{1}{2T}[\bar{E}(t - \tau/2) - \bar{E}(t - \tau/2 - 2T)\exp(i\omega_m 2T)] + i\omega_m \bar{F}_1(t),$$

$$\frac{d}{dt}\bar{F}_2(t) = \frac{1}{2T}[\bar{F}_1(t - \tau/2) - \bar{F}_1(t - \tau/2 - 2T)\exp(i\omega_m 2T)] + i\omega_m \bar{F}_2(t). \tag{9}$$

Then, $\bar{F}(t) = \hat{\sigma} \exp(-i\omega_0 \tau)\bar{F}_2(t)$.

We take into account the Langevin noise sources $\bar{W}_E \equiv (W_+, W_-)$ and $\bar{W}_N \equiv (W_N, W_D)$ that arise from spontaneous emission processes only, because it is not expected that the results depend on the details of the noise process. They have the following form [14]: $W_\pm = \sqrt{\beta_n \Gamma N_\pm}\xi_\pm(t)$ and $W_{(N,D)} = (\Gamma/2\kappa)(W_+^* E_+ \pm W_-^* E_- + \text{c.c.})$, where β_n is the spontaneous emission factor (the normalized fraction of the spontaneously emitted photons that goes into the lasing modes); $\xi_\pm$ are two independent complex noise sources with zero mean and the correlation $\langle \xi_\pm(t)\xi_\pm^*(t')\rangle = 2\delta(t - t')$. In numerical simulations

TABLE I. Table of parameters.

Parameter	Description
$\kappa=300\ \mathrm{ns}^{-1}$	Mean field decay rate
$r_2=0.9975$	Outcoupling mirror reflectivity
$\tau_{in}=28$ fs	Laser cavity round-trip time
$\Gamma=1\ \mathrm{ns}^{-1}$	Decay rate of total carrier population
$\alpha=5$	Linewidth enhancement factor
$\gamma_a=0.5\pi\ \mathrm{ns}^{-1}$	Anisotropic field loss rate
$\gamma_p=25\pi\ \mathrm{ns}^{-1}$	Linear birefringence of medium
$\gamma_s=40\ \mathrm{ns}^{-1}$	Decay rate for difference D
$\sigma_x=60\ \mathrm{ns}^{-1}$	Feedback strength for x axis
$\sigma_y=10\ \mathrm{ns}^{-1}$	Feedback strength for y axis
$\tau=1.4$ ns	External cavity round-trip time
$\beta_n=10^{-5}$	Spontaneous emission factor
$\Delta t=10$ ps	Noise-constant interval
HWHM$=24\pi$ GHz	Filter half width at half maximum
$k_\mu=2\pi\times 600$ GHz	Normalized thermal frequency drift

they are represented as $\xi_\pm(t)=\chi_\pm/\sqrt{\Delta t}$, where $\chi_\pm$ are complex Gaussian random variables (with zero mean and standard deviation $\langle\chi_i\chi_i^*\rangle=2$), and Δt is the time interval over which the noise is held constant.

To integrate numerically the model equations, a fourth-order variable-step method has been used. Typical values of the parameters that have been taken for the numerical simulations of the time evolution of the system are presented in Table I. The value of k_μ corresponds to a frequency drift of $k_J=100$ GHz/mA for a threshold current of $J_{th}=6$ mA [10].

Normalization. The analysis performed below is performed conveniently in normalized variables. Hence we introduce w as the normalized value of the operating frequency,

$$w = T(\Omega - \omega_m). \tag{10}$$

Correspondingly, $w_0^{th}=T(\Delta\omega_0^{th}-\omega_m)$ denotes the normalized initial detuning between the (average) cavity resonance and the grating at the threshold of the solitary laser. Then the normalized detuning, w^m, for a linearly polarized state is given by

$$w^m = T[\Delta\omega_0 - \omega_m - (-\alpha\gamma_a + \gamma_p)(-1)^l], \tag{11}$$

where $l=0(1)$ corresponds to $\hat{x}$- ($\hat{y}$-) polarized states. Similar the normalized initial detuning, Δ, for a linearly polarized state is

$$\Delta = w_0^{th} - T\left[-\left(\alpha - \frac{k_\mu}{\kappa}\right)\gamma_a + \gamma_p\right](-1)^l = w^m + \frac{k_\mu}{\kappa}m. \tag{12}$$

Here, we introduced in addition the normalized values for the injection current (m) and for the population inversion (n):

$$m \equiv T[\kappa(\mu - 1) - (-1)^l\gamma_a], \tag{13}$$

$$n \equiv T[\kappa(N - 1) - (-1)^l\gamma_a]. \tag{14}$$

Finally, a normalized feedback strength is

$$\Lambda \equiv \sqrt{1+\alpha^2}T\sigma. \tag{15}$$

Note that it includes the filter bandwidth and does not depend on the filter shape. It also includes phase-amplitude coupling.

Steady states (monochromatic solutions) of the system (1) and (5) in the absence of noise are found in the form $E_\pm = Q_\pm e^{\pm i\psi + i\Omega t}$. Generally, they can be linearly polarized as well as elliptically polarized. Below, we consider the case of a strong linear birefringence of active medium when the synchronization of the two linearly polarized components of the field is difficult. In that situation, the x- and y-linearly polarized steady-state solutions (or external cavity modes) are more typical. They were given in [10] and are reproduced in normalized form in the Appendix.

III. RESULTS

In this section, we concentrate on presenting and discussing the results that are based on analytical calculations reproduced in the Appendix.

Section III A is devoted to the consideration of the steady state solutions (external cavity modes). Introducing their envelopes as the geometrical locations of the steady-state points with extremal gain or frequency in the spaces $(\Delta\omega_0, N)$ or $(\Delta\omega_0, \Omega)$, we connect the bistability of the envelopes with the bistability between an emission state strongly affected by the feedback and the solitary laser state. Then, we show when this bistability occurs between the nonlasing state and a high-amplitude grating-controlled state (on-off bistability) and an abrupt turn-on of the laser can be observed.

Conditions for bistability are analyzed in Sec. III B. It is shown, that they depend only on two generalized parameters of the system and on the filter shape. Complementary considerations of the laser threshold yield the regions of on-off bistability and the conditions for maximizing the jump of amplitude at the abrupt turn-on event.

In Sec. III C, we investigate stability properties of the external cavity modes and suggest a way to increase the hysteresis loop by a control of the feedback phase. Results of numerical simulations are presented in order to elucidate the findings.

A. Steady-state solutions and simulations: Basic scenario

The envelope approximation. The analysis starts with a calculation of the steady-state solutions. A typical example is presented in Fig. 1(a), where we analyze the space spanned by the solitary laser frequency $\Delta\omega_0$ and the output laser frequency Ω, and Fig. 1(b), where we display the space spanned by the frequency $\Delta\omega_0$ and the total population inversion N. In the printed version, dark gray lines (red and green for x- and y-polarized modes in the online version) denote the location of modes satisfying the threshold condition $\mu\geq\mu_{th}$ or $m\geq m_{th}$ as given by Eqs. (4) and (A14). In the domain

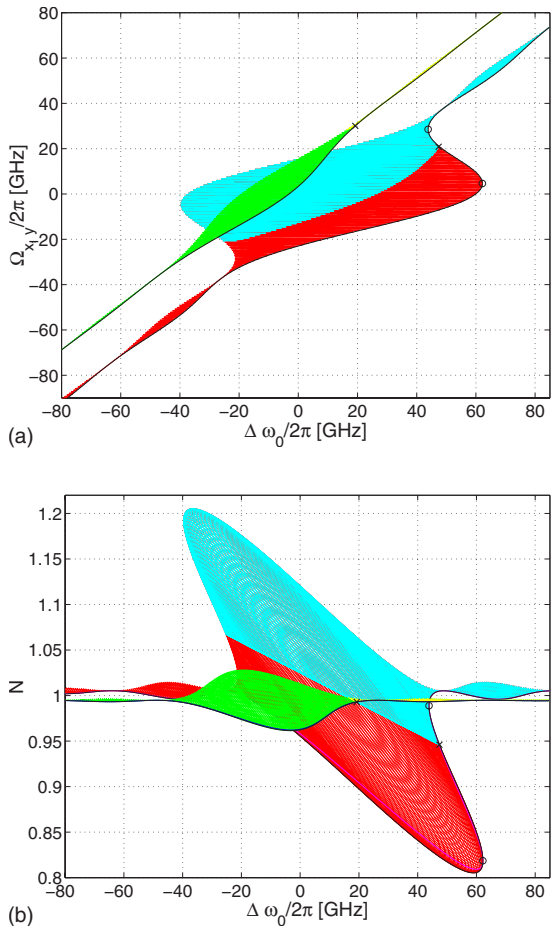

FIG. 1. (Color online) Sets of the steady states in the domains (a) $(\Delta\omega_0,\Omega)$ and (b) $(\Delta\omega_0,N)$. Dark gray lines in the printed version (red and green lines for x- and y-polarized modes in the on-line version) denotes lasing modes (above threshold). Black lines denote $\mathbf{Ew}^{\mathbf{l}}$ and $\mathbf{En}^{\mathbf{l}}$ envelopes, open circles (○) and crosses (×) denote limit and threshold points in the envelope approximation. $\Delta\omega_0^{\mathrm{th}}=30\pi$ ns^{-1}, $\omega_0\tau=0$, $\omega_m=0$ other parameters are given in the text.

$(\Delta\omega_0, N)$, the threshold line has the simplest shape: $\Delta\omega_0=\Delta\omega_0^{\mathrm{th}}-k_\mu(N-1)$.

The envelopes of the steady state sets in the spaces $(\Delta\omega_0, N)$ or $(\Delta\omega_0, \Omega)$ are the geometrical locations of the extremal (maximal or minimal) steady-state points in the corresponding space. They are calculated in the Appendix; see Eqs. (A19) or (A22) and (A23). The black lines in Fig. 1 denote the $(\Delta\omega_0, \Omega)$- and $(\Delta\omega_0, N)$-lower envelopes ($\mathbf{Ew}^{\mathbf{l}}$ and $\mathbf{En}^{\mathbf{l}}$ correspondingly), which are considered below in more detail.

Bistability. The envelopes $\mathbf{Ew}^{\mathbf{l}}$ and $\mathbf{En}^{\mathbf{l}}$ in Figs. 1(a) and 1(b) are S-shaped. The two limit points are denoted by open circles (○) and are obtained from Eqs. (A19) and (A27). Hence, in the area between the two limit points there is the possibility of bistability between two different emission states with the same polarization. One is strongly affected by the feedback, whereas the other one corresponds essentially to the emission of the solitary laser [see the frequencies in Fig. 1(a)]. In between there is a third steady-state solution which is always unstable (the two others might be stable or unstable depending on parameters).

Crosses (×) denote the threshold points where the laser switches on, if the current is increased from zero. They are given by Eqs. (A35) and (A36) under the condition $m=n$. In the domain $(\Delta\omega_0, N)$, the determination of threshold is particularly simple: For the nonlasing solution, increasing the current corresponds to a movement along the line $N=-\Delta\omega_0/k_\mu+1+\Delta\omega_0^{\mathrm{th}}/k_\mu$ starting in the lower right corner. The threshold is encountered where this line intersects with the envelope of the set of steady states. The slope is given by $-1/k_\mu$ which is fixed for a specific device, but the threshold can be varied by changing the threshold solitary-laser frequency $\Delta\omega_0^{\mathrm{th}}$, which corresponds to moving the line up and down. In particular, it can be arranged that the threshold point is between the two limit points. In that case, there is bistability between the feedback-effected state and the off-state between the threshold point and the right limit point. An abrupt (subcritical) turn-on of the laser is encountered to a high-amplitude emission because the threshold steady-state (cross) is unstable and the laser moves to the state on the lower envelope.

Numerical simulation. The above statement becomes more obvious by looking at Fig. 2. It is presenting the evolution of the averaged intensities and of the averaged frequencies for the E_x- and E_y-polarized components, when the injection current is increased or decreased. The analytically obtained steady-state set is superimposed in the same plot. Figure 2 demonstrates that the off-state becomes unstable at about $\mu\approx 0.946$, where an antimode with the minimal intensity collides with the off-state, but that lasing x-polarized external cavity modes appear considerably below this threshold at $\mu\approx 0.9213$. At that point, a saddle-node bifurcation occurs in the phase space far above the zero intensity level resulting in the appearance of a mode and an antimode. If the injection current is increased, more and more modes arise and the region in phase space with external cavity modes expands. As it is shown below, the modes with maximal intensities are stable as a rule. As indicated, the nonlasing off-state is also stable up to the threshold point. In between, there is bistability between the stable nonlasing state and stable lasing states of finite amplitude.

For increasing pump current, the averaged laser intensity is approximately equal to zero (i.e., showing only spontaneous emission noise) up to the threshold point. Then the x-polarized component switches on rather abruptly to a high-amplitude state (Fig. 2, lowermost panel). After that, the intensity of the x-polarized component decreases gradually again because the operating frequency shifts away from the frequency of the grating. The laser stays in the grating-controlled regime with significant amplitude roughly as long the operating frequency remains within the bandwidth of the filter. Obviously, the jump of the intensity at turn-on event is maximal (optimal) or minimal (zero) in the envelope approximation, when the threshold point coincides with the left (right) limit point of Fig. 1.

The uppermost panel of Fig. 2 shows that the switch-on of the laser is accompanied by a significant frequency shift of the laser (below the switch-on the frequency is the peak of the amplified spontaneous emission at the cavity resonance). At this point, the laser goes from freely running operation into the grating-controlled regime. Within the grating-

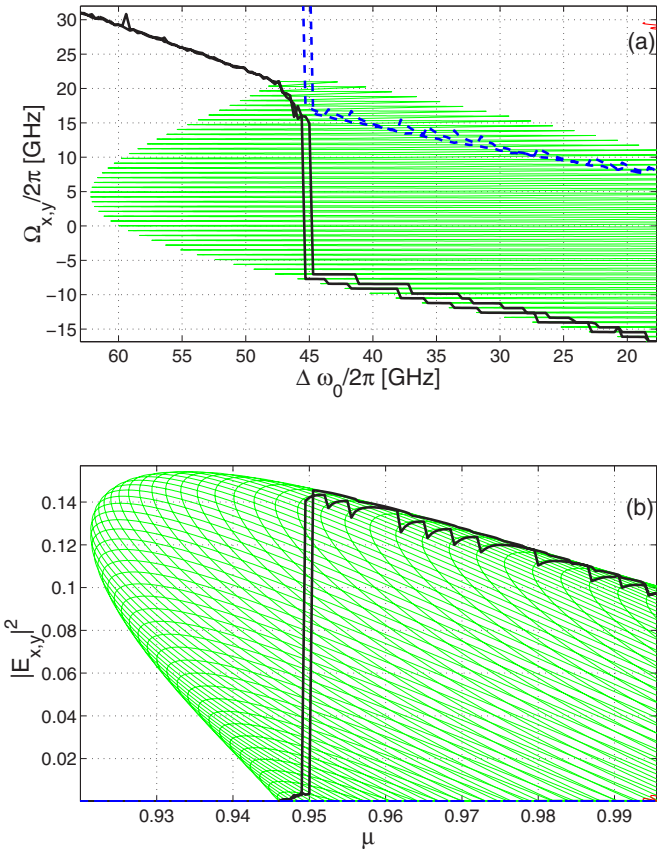

FIG. 2. (Color online) Evolution of the averaged intensities ($\langle|E_x|\rangle^2$ and $\langle|E_y|\rangle^2$) and of the averaged frequencies ($\langle\Omega_x\rangle$ and $\langle\Omega_y\rangle$) for E_x- and E_y-polarized components (averaging time is 200 ns with sampling step 0.08 ns) versus (b) injection current or (a) frequency $\Delta\omega_0$. The thick solid and dashed curves denote the results obtained from numerical simulations for the x and y component, respectively (in the online version the curves for the x and y component are black and blue, respectively). The thin lines denote the analytically obtained steady-state solutions (x: light gray in print version; green in online version). $\beta_n=10^{-5}$, the other parameters are the same as for Fig. 1.

controlled regime, the shift rate of emission frequency with current is changed in comparison to the one for the freely running regime.

Some details of this scenario and the complications due to polarization effects are discussed in [10]. This work gives also experimental evidence for the abrupt turn-on as well as the change in frequency involved. It is the purpose of the present paper to study these transitions analytically in the envelope approximation.

B. Bistability condition

Domains of bistability. Figure 3(a) presents the bistability domain in the space spanned by the normalized full detuning w^m and the normalized feedback strength Λ. The left (right) curve ($\mathbf{B}^{\mathbf{l}}$ and $\mathbf{B}^{\mathbf{r}}$) [calculated from Eqs. (A19) and (A27)] contains the left (right) limit point of the bistable envelope (Fig. 1). They correspond to situations were the jump of the intensity at the abrupt turn-on event is maximal (or minimal,

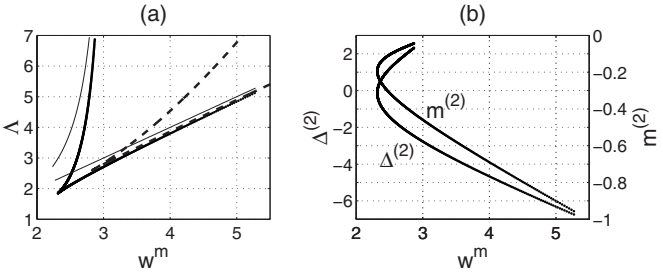

FIG. 3. (a) Bistability boundaries in the space spanned by the normalized full detuning w^m and the normalized feedback strength Λ for the double reflection from the grating (thick lines) with their asymptotes (thin lines) and for an Lorentzian filter (dashed lines). (b) The normalized initial detuning Δ and the normalized threshold current m vs w^m for the case when the laser threshold coincides with the bistability boundaries of (a) in accordance with Eqs. (A45) and (A46) for the parameters of Fig. 1.

i.e., zero). The shape of the bistability domain in the normalized parameter space (w^m,Λ) does not depend on any parameter of the system and is a function of the filter shape $\Pi(w)$ only. Asymptotic expression for the domain boundaries for the case of a high normalized feedback strength are presented in the Appendix. The corresponding curves are depicted by thin lines in Fig. 3(a). The bistability domain for a Lorentzian filter ($\Pi(x)=1/\sqrt{1+x^2}$) is shown also for comparison.

According to the bistability condition (A30), bistability can be found (in an appropriate interval of the initial detuning) only, if the normalized feedback strength is greater than a value $\Lambda_{\min}=1/y_1$ determined by the filter shape only. In Fig. 3(a), this bistability threshold $\Lambda_{\min}$ can be identified as the minimal value of Λ where the curves emerge. The corresponding numerical values for the case of double reflection from the grating (Littman configuration), a single reflection from the grating (Littrow configuration) and for a Lorentzian filter are $\Lambda_{\min}\approx 1.9$, 2.3, and 2.6, respectively. Reformulated for the original variables, the bistability condition (A30) reads

$$\frac{\sqrt{1+\alpha^2}\sigma}{\mathrm{HWHM}} \geq \frac{1}{x_0 y_1}, \tag{16}$$

where the variables on the right hand side are again only determined by the filter profile. The corresponding numerical values for the case of the Littman configuration, the Littrow configuration and for a Lorentzian filter are $1/(y_1x_0)=1.848$, 1.648, and 2.598, respectively. Equation (16) confines the values of the feedback strength (σ), of the filter width (HWHM) and of the line-width enhancement factor (α). The interval of values of the frequency $\Delta\omega_0$ where the bistability exists increases with increasing feedback strength and increasing linewidth enhancement factor, and with narrowing the grating bandwidth.

Equation (A33) connects the averaged frequency shift rate in the grating controlled regime r^{-1} with the normalized feedback strength Λ [Eq. (15)]. More exactly, r is the ratio of the frequency shift rates in the free running and in the grating controlled regimes and can be easily found in the experi-

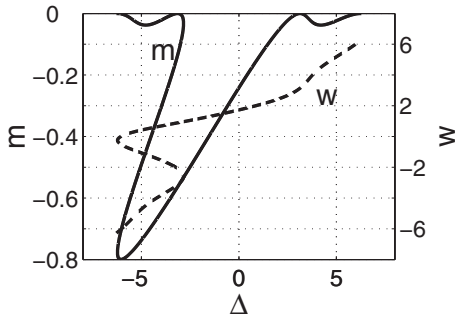

FIG. 4. The normalized threshold injection current m vs the normalized initial detuning Δ (solid line) and the corresponding normalized output laser frequency w (dashed line) for $\Lambda=4.08$ ($\lambda=0.8$) in accordance with Eqs. (A35) and (A36); the other parameters are the same as for Fig. 1.

ment. For this characteristic, the bistability condition can be written in a very simple form $r \geq 2$ [Eq. (A34)]. In the above mentioned experiment [10] the ratio r was about 2.5. Hence the observed shift rate and the observation of bistability are self-consistent.

Threshold conditions. To find the domain of bistability between the off-state and a grating-controlled state (denoted short as on-off bistability domain in the following) we have to add the threshold conditions determined by Eqs. (A35) and (A36) to the above considerations. Figure 4 presents the normalized threshold injection current m and the corresponding normalized output laser frequency w versus the initial detuning Δ for the normalized feedback strength $\Lambda=4.08$ for the parameters of Fig. 1 (for the x-polarized component). The functional forms of the threshold conditions (A35) and (A36) in the space (Δ,m) and of Eqs. (A22) and (A23) for the envelope curve $\mathbf{E}_\mathbf{n}^\mathbf{l}$ in the space (w^m,n) are the same. The only difference is that the parameter α is replaced by α'. The numerical values of the parameters used here are $\alpha=5$ and $\alpha'=-7.6$. Hence the main minimum in the (Δ,m) domain (Fig. 4) is somewhat more pronounced and is slanted in the opposite direction compared to the curve $\mathbf{E}_\mathbf{n}^\mathbf{l}$ in the space (w^m,n) (Fig. 1). Obviously, bistability exists only in a limited interval of initial detunings. A change in slope of the operating frequency versus initial detuning is also apparent in the grating controlled region.

On-off bistability regions. Finally, Fig. 5 combines the bistability domain in the (Λ,w^m) space (black bold curves) and the threshold curves ($\mathbf{T}$) corresponding to different initial detuning Δ. The threshold curves presented in the figure can be divided into four groups depending on the value of the initial detuning Δ. The first group (curves 1, 2, 3, 4) includes curves touching the right bistability boundary ($\mathbf{B}^\mathbf{r}$) and intersecting the left one ($\mathbf{B}^\mathbf{l}$) (see the Appendix for details). The corresponding normalized detunings are smaller than a critical detuning $\Delta^{(3)}$ ($\Delta<\Delta^{(3)}$) given by Eq. (A47) (the reason for this notation will become clear below). The on-off bistability domain for these detunings is situated between the right bistability boundary $\mathbf{B}^\mathbf{r}$ and the threshold curve $\mathbf{T}$ above (and to the right of) the contact point. The latter is the on-off bistability threshold for a fixed initial detuning Δ. At this point, the conditions for the bistability

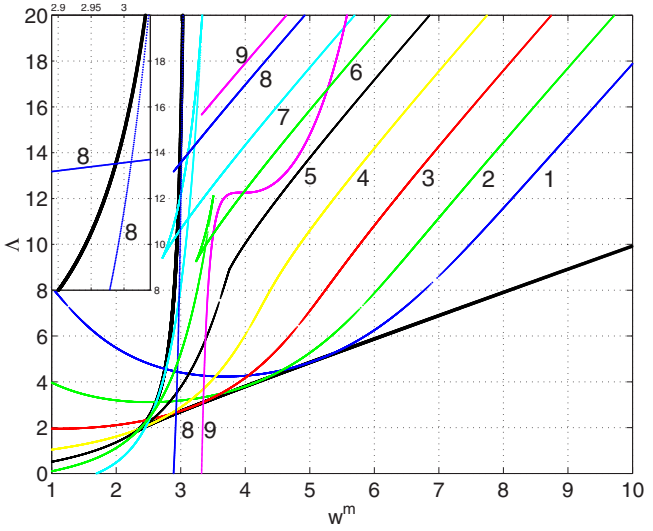

FIG. 5. (Color online) Bistability domain in the space spanned by the normalized feedback strength Λ and the normalized full detuning w^m (thick line), and threshold curves (thin lines) corresponding to different normalized initial detuning Δ in the same parameter space. The curves $1,2,\ldots,9$ correspond to $\Delta=[-6.45,-4.82,-3.19,-1.56,-0.1333,0.83,1.69,2.89,3.32]$. (For comparison, the frequency $\Delta\omega_0^{\text{th}}=30\pi$ GHz^{-1} from Fig. 1 corresponds to the normalized detuning $\Delta=-2.45$.) The other parameters are the same as for Fig. 1. The inset shows an enlargement around the point of self-intersection of curve 8.

boundary and for the threshold curve coincide, i.e., it corresponds to a codimension-2 point requiring the tuning of two parameters. Hence we denote it by $(w^{m(2)}, \Lambda^{(2)})$ (the corresponding value of the detuning Δ is denoted as $\Delta^{(2)}$). It is given by Eqs. (A45), (A19), and (A27). The point corresponds to a transition between supercritical and subcritical (below or above the point, respectively) turn-on behavior, where the jump of the laser intensity is still zero at the codimension-2 point. For stronger feedback levels Λ, the threshold curves $\mathbf{T}$ tend to the asymptotic line given by Eq. (A40)).

For the initial detuning $\Delta=\Delta^{(3)}$ the threshold curve $\mathbf{T}$ (curve 5) passes through the bistability threshold (or the cusp point). The superscript (3) indicates that a tuning of three parameters is necessary to achieve this situation.

The third group of threshold curves ($\mathbf{T}$) with $\Delta^{(3)}<\Delta<\pi$ (curves 6, 7, 8) touches the left bistability boundary ($\mathbf{B}^\mathbf{l}$) and intersects the right one ($\mathbf{B}^\mathbf{r}$). [For the curves 6 and 7, the points of contact are rather close to the cusp of the bistability curve $\mathbf{B}$ and difficult to resolve in Fig. 5. The corresponding values of $w^{m(2)}$ can be retrieved also from Fig. 3(b). For the curve 8, this point is outside the displayed region at $\Lambda\approx 29.9$.] Again, the threshold $\mathbf{T}$ is supercritical below the point of contact $(w^{m(2)},\Lambda^{(2)})$ and subcritical above. The asymptotic behavior for strong feedback is in agreement with Eq. (A40).

In some interval of Δ, these curves contain a point of self-intersection creating a loop with the shape of a swallowtail [curves 5, 6, 7; see Appendix for details; in curve 5 the swallowtail loop is very small but present at the kink around $(w^m,\Lambda)\approx(3.75,8.9)$]. This intersection is denoted by

(w_c^m, Λ_c) and arises at $\Lambda \geq \sqrt{1+\alpha^2}/z_1$ due to a swallowtail catastrophe. [Here, z_1 is again a constant determined by the filter shape only; see Eq. (A44) and the subsequent discussion for details.] Curve 5 depicts the situation just beyond the catastrophe took place.

The "swallowtail triangle" disappears starting from the lower angle when the detuning increases between values corresponding to the curve 7 and 8, but the point of self-intersection persists as a point of intersection of two branches of the curve. For curve 8, one of the branches is hardly distinguishable from the $\mathbf{B^l}$ curve, both running almost vertically on the scale of the full frame of Fig. 5. It is—as well as the point of self-intersection at $(w_c^m, \Lambda_c) \approx (3.0, 13.6)$—resolved in the inset. For curve 9, the point of self-intersection is at $(w_c^m, \Lambda_c) \approx (5.8, 23.8)$, i.e., outside of the range of the figure. The destruction of the swallowtail loop is related to the fact that the threshold curve is only defined with respect to the lower envelope $\mathbf{E_n^l}$ so that one of the branches of the curve 8 and 9 visible in the figure terminates at the points (2.9, 13.2) and (3.3, 15.7), correspondingly. Only the parts of the $\mathbf{T}$ curves to the right of the point (w_c^m, Λ_c) are interesting for our considerations.

A special point $(\Lambda_c^{(2)}, \Delta_c^{(2)})$ is defined by the event when the point of contact $(w^{m(2)}, \Lambda^{(2)})$ coincides with the point of self-intersection (w_c^m, Λ_c). For $\Lambda < \Lambda_c^{(2)}$ and $\Delta < \Delta_c^{(2)}$, the jump of the laser intensity from the off-state is maximal at the point of contact. The on-off bistability domain lies between the curves $\mathbf{B^r}$ and $\mathbf{T}$ above the point of their intersection, i.e., the on-off bistability threshold in this case. For the detunings $\Delta_c^{(2)} < \Delta < \pi$, the feedback strength $\Lambda^{(2)}$ becomes larger than Λ_c, and the point (w_c^m, Λ_c) has to be considered as the exchange point between sub-$(\Lambda > \Lambda_c)$ and super-$(\Lambda < \Lambda_c)$ critical switch-on.

Eventually, for $\Delta > \pi$ (curve 9), the threshold curves $\mathbf{T}$ do not touch the curve $\mathbf{B^l}$ at all, and the corresponding switch-on of the laser is supercritical up to the point (w_c^m, Λ_c) where the supercritical branch of $\mathbf{T}$ intersects the subcritical one with the asymptotic behavior (A40). Above that point the switch-on is subcritical.

For higher values of the normalized feedback strength Λ (which are not shown in the figure) the threshold curves in the considered parameter space can demonstrate a more complex behavior due to the influence of the side maxima of the grating transfer function.

As a summary, Fig. 3(b) depicts the values of $\Delta^{(2)}$ and $m^{(2)}$ versus the normalized full detuning w^m, i.e., the values of the normalized initial detuning Δ and the normalized threshold injection current m where the threshold coincides with the bistability boundaries.

C. Stability of external-cavity modes and phase control

On-off hysteresis. Returning to the numerical simulations displayed in Fig. 2, we see that the high-intensity states cannot be traced far below the switch-on point, if the current is decreased again. The width of the hysteresis loop does not exceed the distance between two adjacent saddle-node points where the corresponding adjacent external-cavity modes disappear. The width of this interval can be roughly evaluated as $2\pi r/(\tau k_\mu)$ (for a variation of current). This means that below the threshold the system prefers—after the destruction of an external-cavity mode by a saddle-node bifurcation—to switch to the stable off-state rather than to the adjacent stable mode with higher intensity, i.e., the trivial off-state is more attractive. The disappearance of the mode by a saddle-node bifurcation is related to the change in the full feedback phase ϕ [determined by Eq. (A12)] accompanying the current-induced frequency shift.

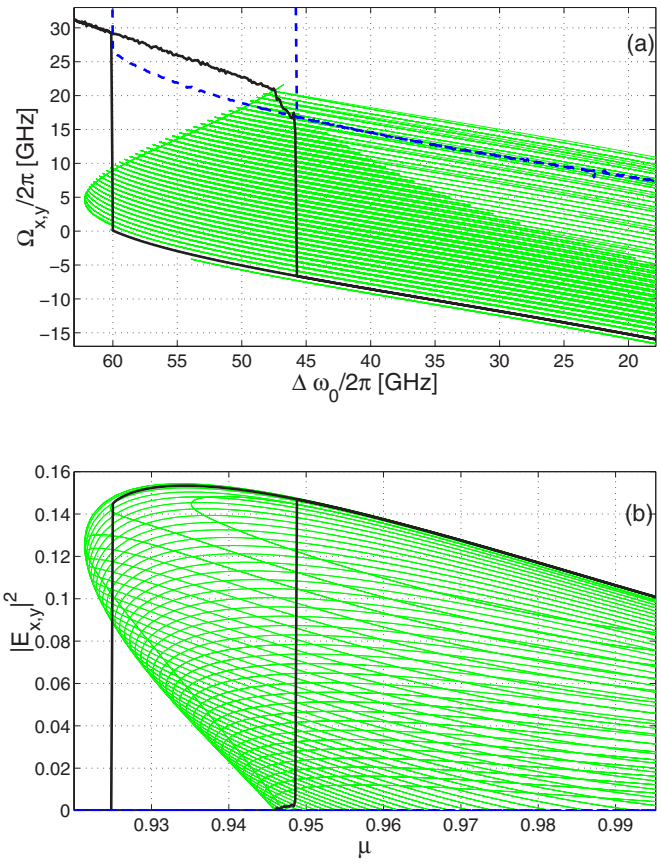

FIG. 6. (Color online) The same as Fig. 2, but with additional phase control in accordance with Eq. (A24).

Hence we investigate the possibility to control the phase $\varphi_0(\mu)$ $(\varphi_0 \equiv \omega_0 \tau)$ in order to keep the system on the same external-cavity mode. This is achieved by making $\varphi_0(\mu)$ current dependent in order to fulfill the condition ϕ_-^n, Eq. (A24), for all currents. In the experiment, this might be implemented using a piezo-electric transducer on the feedback mirror. Results taking into account this phase control $\varphi_0(\mu)$ are shown in Fig. 6. The system evolves close to the $(\Delta\omega_0, N)$ envelope without switchings and hysteresis phenomena on a single external-cavity mode with fixed polarization. The turn-on–turn-off hysteresis loop is much wider than in the case without phase control, its size approaching the maximal possible one given by the distance between the limit and threshold points. Nevertheless, the system switches to the off-state evidently before the limit point at $\mu \approx 0.925$, if the current is decreased (see Fig. 6).

Stability of high-intensity modes. A closer inspection

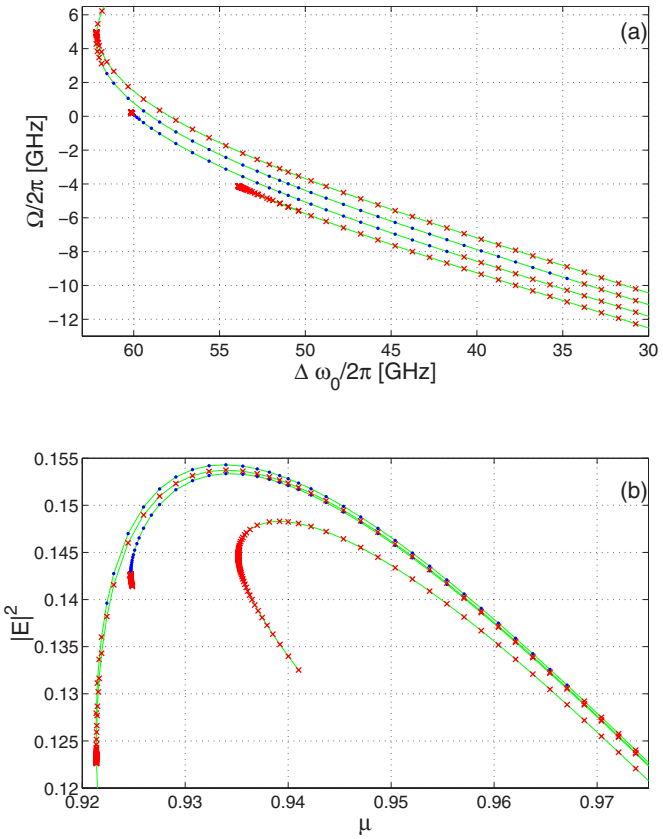

FIG. 7. (Color online) The frequency Ω and intensity $|E|^2$ of external cavity modes (thin lines) and their stability versus frequency $\Delta\omega_0$ (a) or vs μ (b) with additional phase control for the parameters of Fig. 6. Crosses ($\times$) and circles ($\bigcirc$) denote the unstable and stable modes correspondingly.

shows that the system evolves—after the abrupt turn-on—typically not towards the maximal gain mode but to an adjacent one and stays on it on average. For the parameters considered here, this winning mode is the third one labeled according to decreasing power (the maximal gain mode or envelope mode would be the first one in this terminology). It is the second one labeled by the value of the frequency (counting from the mode with minimal frequency). The antimodes are not included in these enumerations because they form continues branches with the corresponding mode. Thus the simulations indicate that the system reaches approximately the saddle-node point for the considered winning mode, if the current is decreased, and again switches off to the more attractive off-state. Let us note that the external-cavity modes displayed in Fig. 6 also obey the phase dependency (A24).

Figure 7 presents the first four external cavity modes with their stability in the $(\Delta\omega_0,\Omega)$ and $(\mu,|E|^2)$ domains when the phase control is turned on. The external-cavity antimodes connected with these modes are also shown partially. Stable solutions are marked by $\bigcirc$ and unstable ones by $\times$. We have calculated Lyapunov exponents for the marked points and give here only the final results regarding the modes stability omitting the details. For convenience, we will denote the mode by two numbers like 1(4) referring to the enumeration using the frequency (intensity) as a reference. For these parameters, the combinations are 1(4), 2(3), 3(1), and 4(2). In the figure, we do not show the complete intervals of μ and $\Delta\omega_0$ analyzed, but for a better visual resolution of the modes we limit the displayed area to a smaller range, though we will discuss the full range.

The minimal frequency mode 1(4) is unstable for all values of current except the small interval of $\mu \in [1.005, 1.00731]$ (or $\Delta\omega_0 \in [12\ \text{GHz}, 10.614\ \text{GHz}]$), being in the close vicinity of the saddle-node bifurcation point of the mode at $\mu \approx 1.00732$ ($\Delta\omega_0 \approx 10.607$ GHz). The winning mode 2(3) is stable for both intervals directly adjacent to its saddle-node points: (1) $\mu \in [1.023, 1.027]$ ($\Delta\omega_0 \in [1.4\ \text{GHz}, -1.4\ \text{GHz}]$); (2) $\mu \in [0.925, 0.956]$ ($\Delta\omega_0 \in [60.2\ \text{GHz}, 41.3\ \text{GHz}]$). The envelope (maximal gain) mode 3(1) is stable for the intervals: (1) $\mu \in [1.08, 1.104]$ ($\Delta\omega_0 \in [-33\ \text{GHz}, -47.3\ \text{GHz}]$); (2) $\mu \in [1.046, 1.061]$ ($\Delta\omega_0 \in [-12.6\ \text{GHz}, -21.5\ \text{GHz}]$); (3) $\mu \in [0.922, 0.968]$ ($\Delta\omega_0$:[61.7 GHz, 34.3 GHz]). The saddle-node point for this mode is $\mu \approx 0.921$ ($\Delta\omega_0 \approx 62.2$ GHz). The mode 4(2) is always unstable.

Attractive mode. Analyzing the stability of the modes for low injection currents $\mu < 1$, we can conclude that the rather wide stability interval for the winning mode 2(3) is included in the even wider stability interval of the envelope mode 3(1). Both these modes are stable for the threshold current corresponding to the abrupt turn-on event. Nevertheless, as the numerical simulations have shown, the redshifted mode 2(3) is more attractive. Moreover, moving along this state, the system frequently displays small oscillations in the vicinity of the mode, which on average give the frequency and intensity of this mode. Comparing the characteristic exponents of the external-cavity modes in their instability intervals, it can be readily observed that the number of the exponents with positive real part (and, for unambiguity, with positive imaginary part) is equal to one for the most reddish mode 1(4). This number reaches two for the winning mode 2(3) for a subinterval of its instability interval, three for the envelope mode 3(1), and four for the mode 4(2). Thus we can conclude that more bluish modes are more unstable in terms of the dimension of the unstable manifold.

It is worth noting, that the switch-on event is a stochastic process and depending on noise-realization different stable final states can be reached though the mode 2(3) seems to have the greatest basin of attraction by far. In particular, we have also observed the transition to the most reddish mode 1(4). If it has been selected in the transient, the system will also remain on it, if the current is changed.

Let us shortly list other qualitative regularities observed for the stability of the modes. (1) Considering the instability of the envelope mode 3(1) for rather high injection currents, we observe that it is connected with perturbations by orthogonally polarized components. (2) For injection currents between the limit point and the left Hopf point of the envelope mode, we could not find stable solutions in numerical simulations even if the phase is varied. (3) In tendency, the chances to find a stable mode are better close to its saddle-node point than far away from it.

Figure 8 demonstrates the typical observation that the mode with maximal or highest gain can be unstable for the

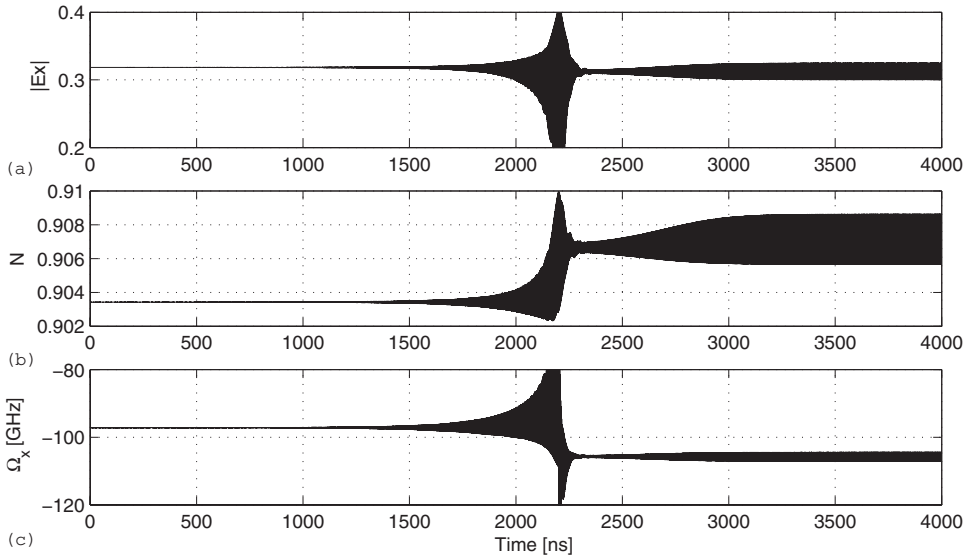

FIG. 8. Transient dynamics. (a) The amplitude of x-polarized component $|E_x|$, (b) the total population inversion N, and (c) the instant frequency Ω_x vs time. The initial conditions are at the mode with maximal gain. The parameters are $\mu=0.995$ and $\beta_n=10^{-8}$; the other parameters are the same as for Fig. 2. The small-amplitude oscillations for large times are an asymptotically stable state.

case of frequency-selective feedback in contrast to conventional feedback [15]. Modes close to the maximal gain mode with smaller gain but lower frequency can be more stable than the maximal gain one. In addition, the smaller gain mode can be also unstable due to a Hopf instability and the system demonstrates small-amplitude periodic oscillations instead of stable emission. This situation is hardly affected by a variation of the feedback phase. For the purpose of demonstration, in Fig. 8 the injection current was chosen to be rather high to be in the domain where all modes are unstable in linear approximation (right-hand side of Fig. 7).

We summarize that the amplitudes of the modes chosen by the system are rather similar to the one of the envelope mode. In addition, the reduction of the bistability domain due to the instability of the envelope mode in the vicinity of the limit point is very small. We demonstrated also that, at least with phase control, the mode structure can be assessed to a great extent. Hence we conclude that the envelope approximation should provide a rather accurate description of the dynamical behavior under consideration.

IV. SUMMARY AND CONCLUSION

In this work, we derived simple analytical conditions for the existence of on-off bistability and the abrupt turn-on in VCSELs with frequency-selective optical feedback in the envelope approximation. In addition, the conditions for achieving a maximal jump of the laser intensity during the abrupt turn-on are elucidated. Contrary to the case of conventional feedback the modes adjacent to the maximal gain one can be more stable. For low injection currents, the vicinity of the lasing limit point can be unstable. Nevertheless, the envelope approximation seems to allow for a good qualitative description of the bifurcation structure. It is demonstrate that the stability properties can be largely altered and wide hysteresis loops can be obtained, if the value of the feedback phase is controlled.

We think that these results are valuable in planning further experiments on bi- and multistability in VCSELs with frequency-selective feedback. From the point of view of self-organization in broad-area lasers, it appears to be interesting to see whether the bistability can lead to localized solutions (cavity solitons), i.e., different emission characteristics in different areas of the device. Another application are photonic devices for all-optical switching.

ACKNOWLEDGMENTS

This work was supported by the Deutsche Forschungsgemeinschaft by travel grants. The recent work of T.A. was supported by the EU-STREP FunFACS. We are grateful for fruitful discussions with K. J. Jentsch on experimental issues.

APPENDIX

Normalization. The normalized value of the frequency (w), the injection current (m), and for the population inversion (n) are defined in Eqs. (10), (13), and (14). In addition, we will use the following definitions, which were partially already introduced in the text, but are repeated for convenience:

$$w_0^{\mathrm{th}} \equiv T(\Delta\omega_0^{\mathrm{th}} - \omega_m), \tag{A1}$$

$$\lambda \equiv T\sigma, \tag{A2}$$

$$\Lambda \equiv \sqrt{1+\alpha^2}\lambda, \tag{A3}$$

$$\alpha' \equiv \alpha - k_\mu/\kappa, \tag{A4}$$

$$\gamma_i \equiv (-\alpha\gamma_a + \gamma_p)(-1)^l, \tag{A5}$$

$$\gamma_i' \equiv (-\alpha'\gamma_a + \gamma_p)(-1)^l, \tag{A6}$$

$$\Delta \equiv w_0^{\mathrm{th}} - T\gamma_i', \tag{A7}$$

$$w^m \equiv \Delta - \frac{k_\mu}{\kappa}m, \tag{A8}$$

$$w^m = T(\Delta\omega_0 - \omega_m - \gamma_i). \tag{A9}$$

Steady-state solutions. The x- and y-linearly polarized steady-state solutions of the model were given in [10]. They are given here in normalized form. The frequency w of a linearly polarized solution is determined from the transcendent equation:

$$w - \Delta + \frac{k_\mu}{\kappa} m = -\lambda\Pi(w)(\alpha\cos\phi - \sin\phi), \tag{A10}$$

where $\Pi(w)$ is the normalized absolute value of the filter reflectivity (the filter shape or the filter profile): $\Pi(w) \equiv |h(w/T+\omega_m)|$, and $\phi \equiv \arg(\mathrm{h}) - \tau(\Omega+\omega_0)$ is the full feedback phase. For the case of a double reflectivity from the grating (Littman configuration), the filter profile is

$$\Pi(w) = (\sin w/w)^2 \tag{A11}$$

and the full feedback phase

$$\phi = -2w - \tau(\Omega + \omega_0). \tag{A12}$$

The steady inversion and the threshold current are

$$n = -\lambda\Pi(w)\cos\phi, \tag{A13}$$

$$m_{\mathrm{th}} = n. \tag{A14}$$

Instead of Eq. (A10), the following equation can be used:

$$w - w^m - \alpha n = \lambda\Pi(w)\sin\phi. \tag{A15}$$

Steady states and threshold curves. The ellipselike curve containing the steady states of the system under consideration in the space (w, n) has the following shape [from Eqs. (A13) and (A15)]:

$$n^2 + [w - w^m - \alpha n]^2 = \lambda^2\Pi^2(w). \tag{A16}$$

Taking into account the threshold condition (A14) gives the following ellipselike curve containing threshold solutions of the system in the space (w, m):

$$m^2 + [w - \Delta - \alpha' m]^2 = \lambda^2\Pi^2(w). \tag{A17}$$

Envelope approximation. The envelopes of the solution (or mode) structure in the spaces (m, w) and (m, n) can be obtained from the corresponding extrema of the curve of steady states (A16). Below, having in mind the relation (A8) between m and w^m, we will frequently identify (m, w) and (w^m, w) spaces and the corresponding envelopes. The same holds for the (m, n) and (w^m, n) spaces and their envelopes. Geometrically, these envelopes can be envisaged as the extrema of the projections of the steady-state surface (A16) in the three-dimensional (w^m, w, n) space onto corresponding two-dimensional subspaces.

(m,w) *envelope*. The envelope **Ew** in the space (m,w) can be found by differentiation d/dn from Eq. (A16) and using $dm/dn = dw/dn = 0$ (or by taking d/dw and using $dn/dw = \infty$ and $dm/dw = finite$). This results in

$$n - \alpha[w - w^m - \alpha n] = 0. \tag{A18}$$

This expression with taking into account Eq. (A16) results in the following equation for the envelope:

$$w - w^m = \pm\Lambda\Pi(w). \tag{A19}$$

Here, the upper and the lower signs correspond to the upper (**Ew$^{\mathbf{u}}$**) and the lower (**Ew$^{\mathbf{l}}$**) boundaries of the mode structure in the space (w^m,w) [or to the maxima and minima for $w(w^m)$]. That is, an arbitrary solution w_a of the system (A13) and (A15) in this space lies between these two envelopes (or boundaries). This can be easily understood also directly from Eq. (A10) leading to

$$|w - w^m| \le \Lambda\Pi(w). \tag{A20}$$

The value of the full feedback phase ϕ corresponding to the real modes belonging to the upper (**Ew$^{\mathbf{u}}$**) and lower (**Ew$^{\mathbf{l}}$**) envelope is the same as for the case of conventional feedback:

$$\phi_\pm^w = (1 \pm 1)\frac{\pi}{2} - \varphi^\alpha \tag{A21}$$

correspondingly, where $\tan\varphi^\alpha = 1/\alpha$.

(m,n) *envelope*. Analogously, the envelope **En** in the domain (m,n) can be found by differentiation d/dw from Eq. (A16) and using $dm/dw = dn/dw = 0$ (or by taking d/dn and using $dw/dn = \infty$ and $dm/dn = finite$), which results in

$$w - w^m = \lambda\Pi(w)[\pm\alpha\sqrt{1 - \lambda^2\Pi'^2(w)} + \lambda\Pi'(w)], \tag{A22}$$

$$n = \pm\lambda\Pi(w)\sqrt{1 - \lambda^2\Pi'^2(w)}. \tag{A23}$$

Again, the upper and the lower signs correspond to the upper (**En$^{\mathbf{u}}$**) and the lower (**En$^{\mathbf{l}}$**) boundaries of the mode structure in the space (w^m,n). These equations can be rewritten using the value of the full feedback phase ϕ corresponding to the modes belonging to the envelope: $\sin\phi^n = \lambda\Pi'(w)$ or

$$\phi_\pm^n = (1 \pm 1)\frac{\pi}{2} - \arcsin\lambda\Pi'(w), \tag{A24}$$

giving expressions similar to those in Eqs. (A10) and (A13):

$$w - w^m = -\lambda\Pi(w)(\alpha\cos\phi^n - \sin\phi^n), \tag{A25}$$

$$n = -\lambda\Pi(w)\cos\phi^n. \tag{A26}$$

Bistability. Now, let us consider the lower envelope **Ew$^{\mathbf{l}}$** (A19) in the space (w^m,w) in more detail. The limit points (or bistability boundaries) are determined by $dw^m/dw = 0$, which results in

$$\Lambda\Pi'(w) = -1. \tag{A27}$$

The limit points lie on the blue side of filter maximum where $\Pi'(w) < 0$, if this derivative of the profile exists. [If not, the limit point corresponds to the point of discontinuity of the derivative $\Pi'(w)$.] Thus the bistability domain is given by the inequality:

$$\Lambda\Pi'(w) \le -1. \tag{A28}$$

To obtain the bistability boundaries (**B**), Eq. (A27) has to be solved along with Eq. (A19). For example, for the case of a

double reflection from the grating, the asymptotic behavior ($\Lambda \to +\infty$) of the boundaries is the following. For $w \to 0$: $\Lambda \sim w^m \sim 3/(2w)$ [right boundary in the domain (w^m, Λ), $\mathbf{B^r}$]. For $w \to \pi$: $\Lambda \sim -\pi^2/[2(w-\pi)]$ and $w^m \sim (\pi+w)/2$, and, therefore, $\Lambda \sim \pi^2/[4(\pi - w^m)]$ [left boundary in the domain (w^m, Λ), $\mathbf{B^l}$]. These are the boundaries associated with the main maximum of the transfer function of the grating. For stronger feedback, analogous bistability boundaries can be found for any side maximum of the grating choosing the normalized frequency w inside the corresponding frequency interval. For the central maximum of an arbitrary filter with a symmetric profile $\Pi(w)$, the asymptotic behavior of the right bistability boundary $\mathbf{B^r}$ in the domain (w^m, Λ) is the same: i.e., at $w \to 0$,

$$\Lambda \sim w^m \sim -\frac{1}{\Pi''(0)}\frac{1}{w}. \tag{A29}$$

This behavior of the right bistability boundary $\mathbf{B^r}$ means that the value of the detuning between the solitary laser frequency and the grating frequency on the boundary tends to the maximal frequency shift $\sigma\sqrt{1+\alpha^2}$ induced by feedback, which is rather obvious.

Bistability condition and frequency shift rate. From the above considerations, we can obtain the bistability condition:

$$\Lambda \geq 1/y_1, \tag{A30}$$

where $y_1 = -\min \Pi'(w)$. It is obtained from $\Pi''(x_1)=0$ as $y_1 = -\Pi'(x_1)$. In other words, the bistability threshold corresponds to $w=x_1$, $\Lambda = 1/y_1$, and $w^m = x_1 + y_2$, where $y_2 = \Pi(x_1)/y_1$. For this point, the right $\mathbf{B^r}$ and left $\mathbf{B^l}$ boundaries touch each other forming a "beak" due to a cusp catastrophe. For the case of a double reflection from the grating considered here and for the main grating maximum $[x_1 \in (0, \pi)]$: $x_1 = 1.30308\ldots$ and $y_1 = 0.540116\ldots$. (The bistability thresholds corresponding to the side grating maxima for stronger feedback are given by the same formula and searching for x_1 in the corresponding frequency intervals.) Hence bistability of the envelope function exists only if the condition (A30) is satisfied. In this case, the bistability domain is determined by Eqs. (A28) and (A19). The bistability condition in unnormalized variables is discussed in the text, Eq. (16).

Introducing $\delta\Lambda = (\Lambda - 1/y_1)y_1$ as a small normalized measure of the feedback strength Λ exceeding the bistability threshold, the bistability boundaries (A27) and (A19) in the vicinity of the cusp point can be approximately expressed as

$$w_{1,2} \simeq x_1 \mp y_3(\delta\Lambda)^{1/2}, \tag{A31}$$

$$w^m_{1,2} \simeq (x_1 + y_2) + y_2\delta\Lambda \pm \frac{2}{3}y_3(\delta\Lambda)^{3/2}, \tag{A32}$$

where $y_3 = \sqrt{2y_1/\Pi^{(3)}(x_1)}$. Here, the indexes "1" and "2" in the left-hand side of the equations correspond to the right ($\mathbf{B^r}$) and left ($\mathbf{B^l}$) bistability boundaries. The first term in Eq. (A32) is the threshold value of the detuning w^m, the second one describes the common shift of the points w^m_1 and w^m_2 at the boundaries $\mathbf{B^r}$ and $\mathbf{B^l}$ with an increase of Λ and the touch of the boundaries in the cusp point, and the third one relates to the relative shift of these points with respect to each other.

After the subcritical switch-on, the laser frequency moves along the envelope on average [see Fig. 2; this takes place on the red side of the filter maximum where $\Pi'(w) > 0$]. So, the shift rate in the grating controlling regime can be roughly approximated as

$$r \equiv \Delta(\Delta\omega_0)/\Delta\Omega \simeq dw^m/dw = 1 + \Lambda\Pi'(w) \simeq 1 + \Lambda y_1. \tag{A33}$$

Here, we have replaced the averaged shift rate by the instantaneous rate, and the latter one by its maximal value. The last equality in Eq. (A33) is correct for a symmetrical profile of the filter. With this definition, the bistability condition (A30) can be rewritten as:

$$r \geq 2. \tag{A34}$$

A mean shift rate more convenient for the measurements would be determined as $\langle r \rangle = (w^m_{\max} - w^m_{\min})/(w_{\max} - w_{\min})$, where $w_{\max}$ and $w^m_{\max}$ could be chosen as the frequency and the detuning exactly after the abrupt switching on event, and $w_{\min}$ and $w^m_{\min}$—as the frequency and the detuning for the state when the laser transits from the grating control regime to the free running operation. Use of the right limit point (w_r, w^m_r) (corresponding to the $\mathbf{B^r}$) instead of the point $(w_{\max}, w^m_{\max})$ results in the lower estimation of the mean rate $\langle r \rangle \simeq 1 + \Lambda K_\Lambda$, where $K_\Lambda = \Pi(w_r)/(w_r - w_{\min})$ with $w_r \in (0, x_1]$ determined from Eq. (A27) [here we neglect by $\Pi(w_{\min})$ which is assumed to be close to 0]. The coefficient $K_\Lambda \sim (1/-w_{\min})[1 - 1/w_{\min}\Pi''(0)\Lambda]$ with $\Lambda \to +\infty$. For the "square sinc" profile, the point $w_{\min}$ can be determined, e.g., as $-\pi$ and the coefficient K_Λ is quickly saturated from the value ≈ 0.123 $(w_r = x_1)$ at the bistability threshold to the value $1/\pi \approx 0.318$ $(w_r = 0)$ with increase of Λ. Taking into account of the real switching on point $(w_{\max}, w^m_{\max})$ together with the fact that for the high values of the feedback strength λ, the envelopes $\mathbf{En^l}$ and $\mathbf{Ew^l}$ (the loci of the maximal gain modes and of the minimal frequency modes, correspondingly) can appreciably differ each from other and that the system tends to evolve more close to $\mathbf{En^l}$, can complicate the estimation of the mean rate $\langle r \rangle$.

Threshold condition. Using Eqs. (A22) and (A23) for the lower envelope $\mathbf{En^l}$ and Eqs. (A8) and (A14), we can obtain the threshold condition in the envelope approximation:

$$w - \Delta = -\lambda\Pi(w)[\alpha'\sqrt{1 - \lambda^2\Pi'^2(w)} - \lambda\Pi'(w)], \tag{A35}$$

$$m = -\lambda\Pi(w)\sqrt{1 - \lambda^2\Pi'^2(w)}. \tag{A36}$$

At a fixed value of the initial detuning (Δ), Eqs. (A35) and (A36) along with Eq. (A8) [or Eq. (A22) with the lower sign] determine the threshold curves $\mathbf{T}$ in the space (w^m, λ). Note that Eq. (A35) is reduced to a quadratic equation with respect to λ^2 with the additional condition $\alpha'(\Delta - w + \lambda^2\Pi\Pi') \geq 0$ (λ and Π are positive by definition). For the case of an arbitrary symmetrical filter profile $\Pi(x)$, the asymptotic behavior of the threshold curves for the main

central maximum $[\Pi''(0)<0,\ \Pi'(0)=0,\ \Pi(0)=1]$ at $w\to 0$ ($\lambda\to+\infty$ and Δ is fixed) is the following:

$$\lambda\sqrt{1+\alpha'^2}\sim\frac{1}{\Pi''(0)}\frac{\alpha'}{w}-\frac{\Delta}{\alpha'}, \tag{A37}$$

$$m(1+\alpha'^2)\sim-\frac{1}{\Pi''(0)}\frac{\alpha'}{w}-\left(\alpha'-\frac{1}{\alpha'}\right)\Delta, \tag{A38}$$

$$w^m(1+\alpha'^2)\sim\frac{1}{\Pi''(0)}\frac{\alpha'(\alpha-\alpha')}{w}+\left(2-\frac{\alpha}{\alpha'}+\alpha\alpha'\right)\Delta, \tag{A39}$$

and, therefore,

$$\lambda\sim\frac{-(1+\alpha\alpha')\Delta+(1+\alpha'^2)w^m}{\sqrt{1+\alpha'^2}(\alpha-\alpha')}, \tag{A40}$$

$$\lambda\sim-\frac{\alpha'}{\sqrt{1+\alpha'^2}}\Delta-\sqrt{1+\alpha'^2}m. \tag{A41}$$

Hence, as for the asymptotic behavior of the (right) bistability boundary $\mathbf{B^r}$ [at $w\to 0$, Eq. (A29)], the asymptotic behavior of the threshold **T** (or switch-on event) for strong filtered feedback in the space (unnormalized feedback strength σ, threshold solitary-laser frequency $\Delta\omega_0^{\mathrm{th}}$ and/or injection current μ) does not depend on the filter bandwidth and shape and can be obtained from simple geometrical considerations [e.g., starting from Fig. 1(b)]. Physical considerations put the following limitations on the parameters: $\alpha>0$, $\beta\equiv k_\mu/\kappa=\alpha-\alpha'>0$. The asymptotic expressions (A37)–(A39) are valid for the case $\alpha'<0$ and $w>0$ or for the case $\alpha'>0$ and $w<0$. The first case corresponds asymptotically to the subcritical threshold (abrupt switch-on) and the second one to the usual supercritical threshold. (The value of α', see Eq. (A4), considered in the numerical section is $\alpha'=5-4\pi\approx-7.6$ in accordance with [10]. Therefore, the main attention is put to the case $\alpha'<0$.) Comparing Eqs. (A40) and (A29), we can conclude that the slope of the asymptotic threshold line **T** is always greater than the one for the right bistability line $\mathbf{B^r}$ in the space (w^m,λ) (with respect to the w^m axis), except for the case $\alpha'=-1/\alpha$ when these angles are equal to each other. Hence, for the case $\alpha'<0$, the domain of on-off bistability is asymptotically between these two lines in the space (w^m,λ). More exactly, the domain can be found between the right bistabilty boundary $\mathbf{B^r}$ described by Eqs. (A27) and (A19) and a part of the threshold curve **T** obtained from Eqs. (A35).

Metamorphoses and catastrophes of the envelopes. Let us start from some rather obvious characteristics of the envelope **En**. The fact that the square root in the Eqs. (A22) and (A23) for the (w^m,n) envelope **En** is defined only for positive arguments leads to restrictions on the possible values of the frequency w for the case $\lambda\geq 1/y_1$, namely $|\Pi'(w)|\leq 1/\lambda$. For lower values of the filtered feedback strength ($\lambda<1/y_1$), the lower $\mathbf{En^l}$ and upper $\mathbf{En^u}$ branches of the envelope are continuous functions of the frequency w, and the normalized inversion $n(w)$ vanishes together with $\Pi(w)$ only. This is the situation depicted in Fig. 1. For stronger

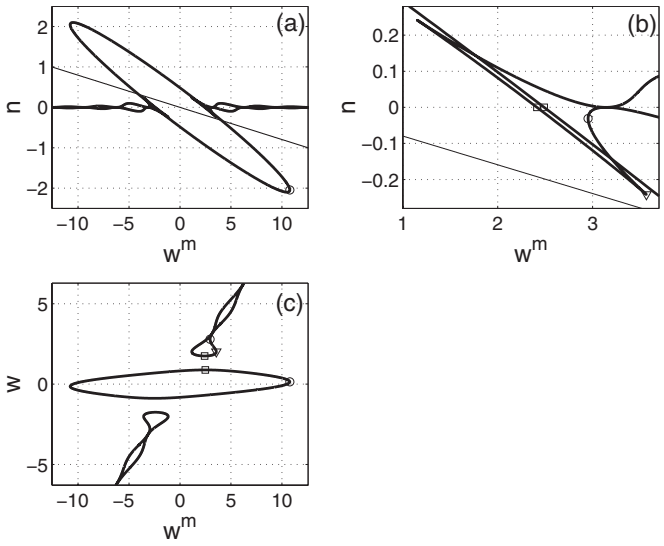

FIG. 9. The envelopes **En** in [(a) and (b)] the domain (w^m,n) and in (c) the domain (w^m,w) for $\lambda=2.1$ (thick lines) calculated by Eqs. (A22) and (A23). The thin line in (a) and (b) is the threshold line for $\Delta=0$ [Eqs. (A8) and (A14)]. Other parameters are given in the text. Open circles (○) denote limit points calculated by Eq. (A27), the triangles gives the limit point [Eq. (A43)] arising due to the envelope metamorphoses, and squares denote the points where $\mathbf{En^l}$ and $\mathbf{En^u}$ are joined due to the metamorphoses.

levels of feedback, the lower $\mathbf{En^l}$ and upper $\mathbf{En^u}$ branches of the envelope corresponding to the opposite signs of Eqs. (A22) and (A23) are joining each other at the points w_j: $|\Pi'(w_j)|=1/\lambda$ [see Fig. 9(a) and the enlargement in (b)]. As a result a gap in frequency values w is formed for which $|\Pi'(w)|>1/\lambda$ and the envelope $\mathbf{En^l}$ is not defined [see Fig. 9(c)]. Let us denote the left point w_j as w_{j1} ($0<w_{j1}<x_1$) and the right one as w_{j2} ($w_{j2}>x_1$). The corresponding values of the inversion n and of the detuning w^m in the points w_j are: $n=0$ and $w_j^m=w_j+\lambda\Pi(w_j)$ [for $w_j>0$ and $\Pi'(w_j)<0$], at which $w_{j2}^m<w_{j1}^m$. [The equations for these points are equivalent to Eqs. (A27) and (A19) for the bistability boundaries with the replacements: $\Lambda\to\lambda$, $w\to w_j$, $w^m\to w_j^m$. See also the corresponding approximations (A31) and (A32) in the vicinity of the cusp.] Thus the envelope curve $\mathbf{En^l}$ in the (w^m,n) domain (for $w^m>0$) splits into (two) continuous parts, "intersecting" each other, with the distance between the parts in w^m-direction approximately determined by $(w_{j1}^m-w_{j2}^m)$, which at the beginning of the splitting is $\simeq(\frac{2}{3})(1/y_3^2)(w_{j2}-w_{j1})^3$, see Figs. 9(b) and 9(c). It can be imagined as a tilted projection of the transparent 3D pinwheel (or spin top) -like surface (A16) when the pinwheel rim partly hides the pinwheel axis. Below, we will be interested in the right point w_c^m ($w_c^m>w_{j1}^m$) of the envelope pseudo-self-intersection $\mathbf{En^l}(w_{c1})=\mathbf{En^l}(w_{c2})$ with $w_{c1}\neq w_{c2}$ [i.e., $w^m(w_{c1})=w^m(w_{c2})\equiv w_c^m$ and $n(w_{c1})=n(w_{c2})\equiv n_c$]. We use the term "pseudointersection" when the intersection of two curves takes place only in the corresponding two-dimensional projection and is absent in the three-dimensional space with the third coordinate w, i.e., the curves have different frequencies w in the point of intersection.

Asymptotically, in accordance with the above considerations [see, e.g., Eq. (A29)], the right point w_{j1}^m of the junc-

tion of envelopes (with $n=0$ and minimal frequency w_{j1}) at $\lambda \to +\infty$ tends asymptotically towards the filtered feedback strength λ:

$$w_{j1}^m \sim \lambda \sim -\frac{1}{w_{j1}\Pi''(0)}. \tag{A42}$$

In this situation, the branch of the envelope **En** with frequency $w \in [-w_{j1}, w_{j1}]$ forms a closed ellipse-like-curve [see Eq. (A16)] and the branch with $w \geq w_{j2}$ ($w^m \geq w_{j2}^m$) forms a continuous curve intersecting the first one. In the presence of additional side maxima of the grating (as for the "square-sinc" profile), stronger levels of feedback lead to analogous metamorphoses of the envelopes near these maxima.

Let us now consider in more detail the events preceding the splitting of the envelops (for $\lambda < 1/y_1$). For that we need to find all possible extremal (limit) points of the $\mathbf{En}^{\mathbf{l}}$ envelope. The derivative dw^m/dw of Eq. (A22) is factored in two multipliers. The zeros of the first one give exactly the limits points considered above for the bistability boundaries [Eq. (A27)]. The zeros of the second multiplier are determined from the following equation:

$$\lambda^2 \frac{1}{2}[\Pi^2(w)]'' = 1. \tag{A43}$$

Analogously, the first multiplier of the derivative dn/dw from Eq. (A23) gives simply the extremal points of the profile function $\Pi(w)$, and the zeros of its second multiplier are exactly determined by Eq. (A43). Equation (A43) has solutions only in the case

$$\lambda \geq 1/z_1, \tag{A44}$$

where $z_1 = \max\sqrt{\frac{1}{2}[\Pi^2(w)]''}$. The corresponding value of the frequency $w=x_s$ can be found from $[\Pi^2(x_s)]^{(3)}=0$. (For the "square-sinc" profile: $x_s=1.54687$ and $z_1=0.581026$.) Thus, when the feedback strength λ exceeds the threshold value $1/z_1$, two additional extremal points (a maximum and a minimum) arise both for the dependency $w^m(w)$ given by Eq. (A22) and for the dependency $n(w)$, Eq. (A23). Since the minimum of one function coincides with the maximum of the other one, and vice versa, the behavior of the envelope **En** in the space (w^m, n) near the corresponding extremal (limit) points has a cusplike shape. These two limit points collide with each other and disappear, when the feedback strength λ tends to the threshold value $(1/z_1)_{+0}$, and the envelope **En** has a swallowtail-like shape here. For the "square-sinc" profile under consideration, the above mentioned self-intersection point (w_c^m, n_c) also arises for this value of the feedback strength λ. Similar as in the vicinity of the bistability cusp point, introducing a normalized deviation $\delta\lambda = (\lambda - 1/z_1)z_1$, the above extremal points of the envelope near the threshold of their appearance are described by formulas analogous to Eqs. (A31) and (A32). In particular, $w \simeq x_s \mp (2/\lambda_s)\{-[\Pi^2(w_s)]^{(4)}\}^{-1/2}(\delta\lambda)^{1/2}$. Geometrically, the formation of the considered swallowtail-like configuration corresponds to the situation when for the projection of the pinwheel-like surface (A16), the pinwheel rim only starts to hide two diametrically opposite points of the pinwheel axis.

With increasing feedback strength λ, one of the cusplike extremal points of $\mathbf{En}^{\mathbf{l}}$ and the corresponding one for $\mathbf{En}^{\mathbf{u}}$ tend to zero level of the normalized inversion n and to each other, up to the value of $\lambda = 1/y_1$ where these envelops are joining and split (see above).

Analogous metamorphoses take place for the threshold dependencies $\Delta(w)$ and $m(w)$, Eqs. (A35) and (A36) (with the replacements $n \to m$, $w^m \to \Delta$, and $\alpha \to \alpha'$), i.e., two additional extremal points arise at $\lambda = 1/z_1$ and $w=x_s$ for these dependencies also. Thus, in the three-dimensional control parameter space (w^m, λ, Δ), the point $\lambda = 1/z_1$ (and $w=x_s$) with the corresponding values of w_s^m and Δ_s [calculated from Eqs. (A22) and (A35)] can be considered as a swallowtail catastrophe point (where two lines of cusp points are meeting). The normalized detunings w_s^m and Δ_s depend only on the profile shape and on the values of α and α'. (For the "square-sinc" profile and the values of α and α' under consideration, $w_s^m \approx 3.793$ and $\Delta_s \approx -0.2355$.)

On-off bistabilty threshold and optimal switch-on. A codimension-two condition occurs when the threshold curves **T** [described by Eq. (A35)] touch the bistability boundaries **B** [determined by Eqs. (A19) and (A27)] which corresponds to the points, where the supercritical switch-on of the laser transforms to the subcritical one and vice versa. The corresponding normalized initial detuning (Δ) can be determined from the following equation:

$$\Delta^{(2)} - w^m = \frac{\alpha}{1+\alpha^2}\frac{k_\mu}{\kappa}(w - w^m), \tag{A45}$$

which has to be solved together with Eqs. (A19) and (A27). The corresponding normalized threshold current (m) is given by

$$m^{(2)} = \frac{\alpha}{1+\alpha^2}(w - w^m). \tag{A46}$$

A codimension-three condition, for which the laser threshold coincides with the bistability threshold (A30), takes place for the following values of initial detuning (Δ) and of injection current (m):

$$\Delta^{(3)} = x_1 + y_2\left(1 - \frac{\alpha\beta}{1+\alpha^2}\right), \tag{A47}$$

$$m^{(3)} = -\frac{\alpha}{1+\alpha^2}y_2, \tag{A48}$$

where $\beta \equiv k_\mu/\kappa$ as defined before.

Thus, the value of initial detuning $\Delta = \Delta^{(3)}$ determines a threshold curve in the space (w^m, λ) passing through the bistability threshold. In the case $\alpha' < 0$, threshold curves with $\Delta < \Delta^{(3)}$ touch the right bistability boundary $\mathbf{B}^{\mathbf{r}}$ (but do not intersect it) and pseudointersect the left bistability boundary $\mathbf{B}^{\mathbf{l}}$. The point of contact $(w^{m(2)}, \lambda^{(2)})$ at $\mathbf{B}^{\mathbf{r}}$ can be determined as an on-off bistability threshold for the fixed initial detuning Δ. That is, the on-off bistability (between lasing and nonlasing state) takes place only for feedback strength $\lambda > \lambda^{(2)}$, in the interval of full detunings w^m (or of injection currents m) between the parts of the threshold **T** and of the bistability $\mathbf{B}^{\mathbf{r}}$

curves above the point. Below the point, the threshold behaviour is supercritical.

The threshold curves with $\Delta > \Delta^{(3)}$ touch the left bistability boundary $\mathbf{B^l}$ (but do not intersect it) and pseudointersect the right bistability boundary $\mathbf{B^r}$. A particular shape of the filter profile can lead to the existence of an upper limit of the detuning ($\Delta_{\max}^{\mathrm{con}}$) for this behavior. For example, for the "double-sinc" profile, the value of w^m (with the frequency value w) on the boundary $\mathbf{B^l}$ asymptotically tends to π (the first zero of the filter profile), and therefore, $\Delta_{\max}^{\mathrm{con}} = \pi$.

Due to the catastrophic metamorphoses of the envelope $\mathbf{En^l}$ and, in particular, due to the existence of the pseudo-self-intersection of $\mathbf{En^l}$ in the point (w_c^m, n_c) for the values of feedback strength $\lambda > 1/z_1$, the corresponding threshold curves $\mathbf{T}$ can pseudo-intersect themselves in the point (w_c^m, λ_c) forming a swallowtail-view loop in the space (w^m, λ), which disappears due to the swallowtail catastrophe when $\lambda_c(\Delta) \to 1/z_{1+0}$. For stronger feedback levels $\lambda \to +\infty$ and small positive frequencies $w \to 0_{+0}$, the threshold curves $\mathbf{T}$ tend to the asymptotic lines (A40).

The optimal condition for the subcritical switch-on event, i.e., the condition where the jump in the intensity is maximal, is achieved in the point of contact $(w^{m(2)}, \lambda^{(2)})$ of the threshold curve $\mathbf{T}$ and the left bistability boundary $\mathbf{B^l}$ for $\lambda < 1/z_1$ and $\Delta \in (\Delta^{(3)}, \Delta_{\max}^{\mathrm{con}})$. The upper limit of the optimum definition can be extended up to the value of $\lambda = \lambda_c^{(2)} > 1/z_1$ when the left limit point of the envelope $\mathbf{En^l}$ coincides with the point (w_c^m, n_c) of its pseudo-self-intersection. The corresponding value of Δ is reached when the threshold $\mathbf{T}$ passes through the point $(w_c^{m(2)}, \lambda_c^{(2)})$: $\Delta_c^{(2)} < \Delta_{\max}^{\mathrm{con}}$. For stronger feedback levels $\lambda > \lambda_c^{(2)}$, this optimum is achieved in the point (w_c^m, λ_c) for $\Delta > \Delta_c^{(2)}$.

[1] F. Favre and D. Le Guen, IEEE J. Quantum Electron. **QE-21**, 1937 (1985).

[2] R. Wyatt and W. J. Delvin, Electron. Lett. **19**, 110 (1983).

[3] E. Brinkmeyer, W. Brennecke, M. Zurn, and R. Ulrich, Electron. Lett. **22**, 134 (1986).

[4] M. Kozuma, M. Kourogi, and M. Ohtsu, Appl. Phys. Lett. **61**, 1895 (1992).

[5] P. Zorabedian, W. R. Trutna, and L. S. Cutler, IEEE J. Quantum Electron. **QE-23**, 1855 (1987).

[6] Chi Yang, X. Wang, and J. G. McInerney, IEEE J. Quantum Electron. **232**, 813 (1996).

[7] M. Giudici, L. Giuggioli, C. Green, and J. R. Tredicce, Chaos, Solitons Fractals **9**, 1 (1998).

[8] A. P. A. Fischer, O. K. Andersen, M. Yousefi, S. Stolte, and D. Lenstra, IEEE J. Quantum Electron. **QE-36**, 375 (2000).

[9] A. Naumenko, P. Besnard, N. Loiko, G. Ughetto, and J. C. Bertreux, IEEE J. Quantum Electron. **39**, 1216 (2003).

[10] A. Naumenko, N. Loiko, M. Sondermann, K. Jentsch, and T. Ackemann, Opt. Commun. **259**, 823 (2006).

[11] M. Sondermann, F. Marino, K. F. Jentsch, T. Ackemann, and R. Jäger, *Nonlinear Guided Waves and Their Applications* (Technical Digest of OSA Topical Meeting, Toronto, 2004), paper MB5.

[12] S. Barland, J. R. Tredicce, M. Brambilla, L. A. Lugiato, S. Balle, M. Giudici, T. Maggipinto, L. Spinelli, G. Tissoni, T. Knodel, M. Miller, and R. Jager, Nature (London) **419**, 699 (2002).

[13] M. San Miguel, Q. Feng, and J. V. Moloney, Phys. Rev. A **52**, 1728 (1995).

[14] J. Mulet, C. R. Mirasso, and M. San Miguel, Phys. Rev. A **A64**, 023817 (2001).

[15] A. M. Levine, G. H. M. van Tartwijk, D. Lenstra, and T. Erneux, Phys. Rev. A **52**, R3436 (1995).